All-Printed Roll-to-Roll Perovskite Photovoltaics Enabled by Solution-Processed Carbon Electrode

David Beynon,* Ershad Parvazian,* Katherine Hooper, James McGettrick, Rahul Patidar, Tom Dunlop, Zhengfei Wei, Peter Davies, Rodrigo Garcia-Rodriguez, Matt Carnie, Matthew Davies, and Trystan Watson*

Perovskite photovoltaics have shown great promise in device efficiency but also the promise of scalability through solution-processed manufacture. Efforts to scale perovskites have been taken through printable mesoporous scaffolds and slot die coating of flexible substrates roll-to-roll (R2R). However, to date there has been no demonstration of entirely R2R-coated devices due to the lack of a compatible solution-processable back electrode; instead, high-value evaporated metal contacts are employed as a post process. Here, in this study, the combination of a low-temperature device structure and R2R-compatible solution formulations is employed to make a fully R2R printable device architecture overcoming interlayer incompatibilities and recombination losses. Therefore, the n–i–p device structure of SnO_2/perovskite/poly(3,4-ethylenedioxythiophene)/carbon is employed to form an ohmic contact between a p-type semiconductor and printable carbon electrode. In particular, the results show that the small-scale device efficiencies of 13–14% are achieved, matching the device performance of evaporated gold electrodes. Also, this entirely R2R-coated perovskite prototype represents a game changer, reaching over 10% (10.8) stabilized power conversion efficiency with unencapsulated long-term stability retaining 84% of its original efficiency over 1000 h under 70% RH and 25 °C.

1. Introduction

The interest in perovskite photovoltaics has been intense due to the well-reported increase in lab-based device performance.[1–3] Since the original reporting of perovskite-based devices[4–6] there has been a rapid rise in device efficiency achieving over 25% power conversion efficiency (PCE, 25.2%).[7,8] In addition to the impressive device performance improvements in lab scale fabrication, perovskite photovoltaics as solution-processed devices have the promise of high scalability through roll-to-roll (R2R) coating processes.[9–13]

Among available coating techniques, the feasibility of perovskite photovoltaic (PV) scaling-up has been mostly investigated through the slot-die coating process.[14–18] This industrially scalable process promises high-speed R2R processing of perovskite PV devices,[19–21] an attractive proposition as when combined with R2R encapsulation large volumes of completed photovoltaics could be fabricated in a single process. Research in this area is growing with feasibility demonstrations conducted on benchtop deposition tools for both p–i–n and n–i–p device stacks.[11,22,23] More recently partly R2R-coated perovskite PV devices have been demonstrated. In one study, a two-step sequential process demonstrated to fabricate slot-die-coated R2R n–i–p devices with a high PCE of 13%.[24] Othman et al. applied a triple-cation mixed halide perovskite in an inverted p–i–n stack using R2R coating for the first time and reached a PCE of 12%.[25] In their work, they also modified the underlying hole-transport layer (HTL) with guanidinium iodide

D. Beynon, E. Parvazian, K. Hooper, J. McGettrick, R. Patidar, T. Dunlop, Z. Wei, M. Carnie, M. Davies, T. Watson
SPECIFIC IKC
Faculty of Science and Engineering
Swansea University
Fabian Way, Swansea SA1 8EN, UK
E-mail: d.g.beynon@swansea.ac.uk; ershad.parvazian@swansea.ac.uk; t.m.watson@swansea.ac.uk

P. Davies
AIM
Faculty of Science and Engineering
Swansea University
Fabian Way, Swansea SA1 8EN, UK
R. Garcia-Rodriguez
IMPACT
Faculty of Science and Engineering
Swansea University
Fabian Way, Swansea SA1 8EN, UK

**ADVANCED
SCIENCE NEWS**

www.advancedsciencenews.com

**ADVANCED
MATERIALS**

www.advmat.de

Table 1. Photovoltaic parameters of R2R-coated perovskite solar cell studies published to date.

	Device structure	R2R layers	Electrode	PCE [%]	Year	Group [Ref]
Semi R2R	PEDOT:PSS/MAPbI$_{3-x}$Cl$_x$/PCBM/ZnO/Ag	All except electrode	Ag (screen-printed)	4.9	2015	DTU Ref. [22]
	PEDOT:PSS/MAPbI$_{3-x}$Cl$_x$/PCBM/ZnO/Ag	All except electrode	Ag (evaporated)	5.1	2015	Zhejiang Uni[23]
	PEDOT:PSS/MAPbI$_3$/PCBM/Ca/Al	PEDOT & perovskite	Ca & Al (evaporated)	11.2	2018	CSIRO/CAS Ref. [28]
	SnO$_2$/Cs$_{0.15}$FA$_{0.85}$PbI$_{2.55}$Br$_{0.45}$/Spiro/Au	SnO$_2$ & perovskite	Au (evaporated)	13.5	2018	Solliance Ref. [29]
	IZO/SnO$_2$/MAPbI$_3$/Spiro/Au	SnO$_2$ & perovskite	Au (evaporated)	14.1	2018	NREL Ref. [30]
	PEDOT:PSS/triple cation psk/PCBM/PEIE/Ag	All except electrode	Ag (evaporated)	11.7	2019	GIST/CSIRO Ref. [21]
	SnO$_2$/MAFACs/Spiro/Ag	SnO$_2$ & perovskite	Ag (evaporated)	9.9	2019	CSU Ref. [31]
	SnO$_2$/MAPbI$_3$/P3HT/Ag	SnO$_2$, PbI$_2$, P3HT	MAI dipped/Ag (evap.)	9.7	2019	KRICT and VTT Ref. [35]
	SnO$_2$/MAFAPbIBrCl/P3HT/Au	All except electrode	Au (evaporated)	13.8	2020	KRICT and VTT Ref. [32]
	PEDOT:PSS/MAPbI$_3$/PCBM/BCP/Ag	All except electrode	Ag (evaporated)	12.2	2020	SPECIFIC Ref. [26]
	PEDOT:PSS/CsFAMAPb(IBr)/PCBM/PEIE/Au	PEDOT:PSS and PSK	Au (evaporated)	12.0	2021	Monash/CSIRO Ref. [25]
	SnO$_2$/FAMAPbI$_3$/PPDT2FBT/C/Cu/Al	All except electrode	C/Cu/Al (pressed foil)	10.0	2021	Monash/CSIRO Ref. [33]
	SnO$_2$/MAPbI$_3$/P3HT/Au	All except electrode	Au (evaporated)	9.87	2021	CNR & VTT Ref. [36]
	ET/TCE/SnO$_2$/CFAMPb(IBr)/Spiro/carbon/Ag	All except electrode	Ag & C (bar coated-pressed)	16.7	2022	CSIRO/Monash Ref. [27]
	SnO$_2$/MAPbI$_3$/Spiro/Ag	All except electrode	Ag (evaporated)	13.0	2022	CSU/CSIRO Ref. [24]
	OPV8/SnO$_2$/FA$_{0.91}$Cs$_{0.09}$PbI$_3$/Spiro/Au	All except electrode	Au (evaporated)	15.42	2022	CSIRO Ref. [34]
Fully R2R	Current study	All	C (slot-die R2R)	10.8	2022	SPECIFIC

additive to form millimeter-sized perovskite clusters. Also, in our previous work,[26] a p–i–n device structure of poly(ethylene terephthalate) (PET)/indium tin oxide (ITO)/poly(3,4-ethylene dioxythiophene):polystyrene sulfonate (PEDOT:PSS)/MAPbI$_3$/[6,6]-phenyl C61 butyric acid methyl ester (PCBM)/bathocuproine (BCP) is demonstrated achieving a PCE of 12.2% with all layers sequentially coated R2R except conductive top electrode. Recently, the potential for a laminated electrode made up of multilayer silver and carbon stack has been demonstrated by applying the electrode onto a R2R-coated stack using a calendar press.[27] These represent important advancements toward the promise of large-area, high-volume solution-processed perovskite devices, and are summarized in **Table 1**.[21–36] However, in almost all R2R perovskite photovoltaic research to date, the final electrode deposition is achieved through evaporation of a precious and limited-resource metal. Although evaporation of gold or silver as a contact electrode enables researchers to fabricate efficient and consistent devices, this slow, expensive, wasteful process is a key barrier to perovskites leaving the lab and finding real world applications. A potential solution to this slow processing and high-cost step is to use a printed solution-based top electrode. Printed carbon electrodes have been proven to be effective in the triple mesoporous architecture,[37–39] where several high-temperature (>450 °C) processing steps are required which are incompatible with the PET film substrates required for R2R processing.[38] Carbon electrodes have also been successfully utilized in planar device architectures at lab scale[40–43] but there are a few major problems inhibiting carbon electrode perovskite solar cells (PSCs) achieving high performance. Zhang et al. overcame the solvent compatibility issue through solvent exchange and hot pressing of dry carbon layers onto the completed devices.[44] Alternative strategies use complex or high-temperature processes such as protecting the perovskite layer using copper thiocyanate[45] or

evaporated interlayers to enable interlayer to carbon electrode integration.[46] In another innovative work,[47] a spray-coated graphene electrode was used on both sides of a modular laminated top contact PSC design, which sheet resistance and thickness were greatly reduced under applied pressure. Due to the complexity, high temperature, or carbon electrode formulation, these solutions are not scalable through R2R processing. To overcome both the scalability and compatibility issue, Sepalage et al. introduced a novel two-component electrode including modified aluminium foil and carbon layer.[48] Although their electrode is compatible with layers underneath and can be pressed or laminated easily, the aluminium foil, on the other hand, cannot be applied for sequential R2R purposes. To achieve a solution-based well-suited R2R carbon electrode, which is compatible with other device layers, an exceptional carbon ink formulation is needed. Formulation of the carbon ink is critical with solvent orthogonality with the device stack as a limiting factor. To enable coating of the full perovskite device stack including the electrode, the device architecture must be designed for process compatibility, i.e., low-temperature processing, layer orthogonality, interlayer alignment, and solvent compatibility.

In this work, we employ a low-temperature n–i–p device architecture in which the typical Spiro-MeOTAD (2,2′,7,7′-tetrakis(N,N-di-p-methoxyphenyl-amine)-9,9′-spirobifluorene) HTL is replaced with a lower cost and humidity/thermally stable PEDOT layer coated directly onto the perovskite. We also formulated a carbon ink fully compatible with the underlying layers of the device structure and rheologically compatible with R2R slot-die coating. This is the first demonstration of fully R2R-coated perovskite cells achieving a stabilized efficiency of 10.84% which compares well to previous reports of R2R-coated devices with evaporated metal contacts (Table 1). In addition, our unencapsulated devices exhibited

enhanced long-term stability compared to typical spiro-MeOTAD/gold PSCs.

## 2. Results and Discussion

2.1. Device Architecture

Achieving R2R PSCs requires a low-temperature solution-based manufacture for all the layers, which can be coated easily on flexible substrates. Tin oxide has been demonstrated as an effective low-temperature-processed electron-transport layer suitable for slot-die coating[29,49] in combination with perovskite and Spiro-MeOTAD layers in PSCs. Along with tin oxide, perovskite precursor dissolved in acetonitrile has been successfully used as an excellent low-toxic ink for R2R coating,[18,26,29,50] however, the main challenge remains coating a top electrode in a continuous, sequential R2R process. To obtain the intended carbon ink formulation, we set three goals: compatibility, conductivity, and scalability.

Ink formulation requires solvent that will challenge compatibility with perovskite, binder that will control rheology for scalability and conductive carbon, which will alter both rheology and conductivity of the dry ink. We first investigated solvent compatibility by soaking coated perovskite layers in candidate solvents for a 24 h period, after this time the samples were visually inspected and analyzed using photoluminescence (PL) spectroscopy (Figure S1a, Supporting Information). Quenching ability of carbon inks formulated from these solvents is shown in Figure S1b in the Supporting Information. 2-Methylanisole showed no colorimetric change and has PL matching that of

the unsoaked perovskite control, it has a suitable boiling point of 170 °C allowing low-temperature curing while remaining wet through processing. 2-methylanisole can be considered a green solvent as there is no significant toxicity and therefore no associated workplace exposure limits making it suitable for scale up and use in large volumes. The ink was therefore formulated by combining 2-methylanisole, ethylcellulose binder, carbon black, and graphite conductive components. Details on how to prepare, develop, and optimize our carbon ink are given in the Experimental Section. The rheology of the ink is critical for successful application therefore two optimized inks are used, a viscous paste for stencil coating and a low-viscosity ink for slot-die coating, both are thixotropic in nature (Figure S2, Supporting Information).

Investigating the potential of the optimized carbon ink formulation, we first evaluated the performance of small-scale spin-coated perovskite devices including carbon top electrode. Devices are fabricated using spin coating of planar n–i–p structures ITO/SnO$_2$/MAPI/carbon and ITO/SnO$_2$/MAPI/Spiro/gold (as device control) where the gold electrode is evaporated, and the carbon electrode is applied by stencil coating a viscous paste. **Figure 1**a and Figure S3 in the Supporting Information show the schematic of carbon coating method and fabricated devices' photographs. To coat the carbon by the stencil method, we first made PET-patterned stencils by laser cutting with identical size and shape as the shadow-mask we use for Au evaporation.

The resultant devices reached champion efficiency of 18.9% for gold electrode; however, the carbon electrode devices produced only around 3% efficiency and depressed J–V characteristics (Figure 1c and Figure S4, Supporting Information).
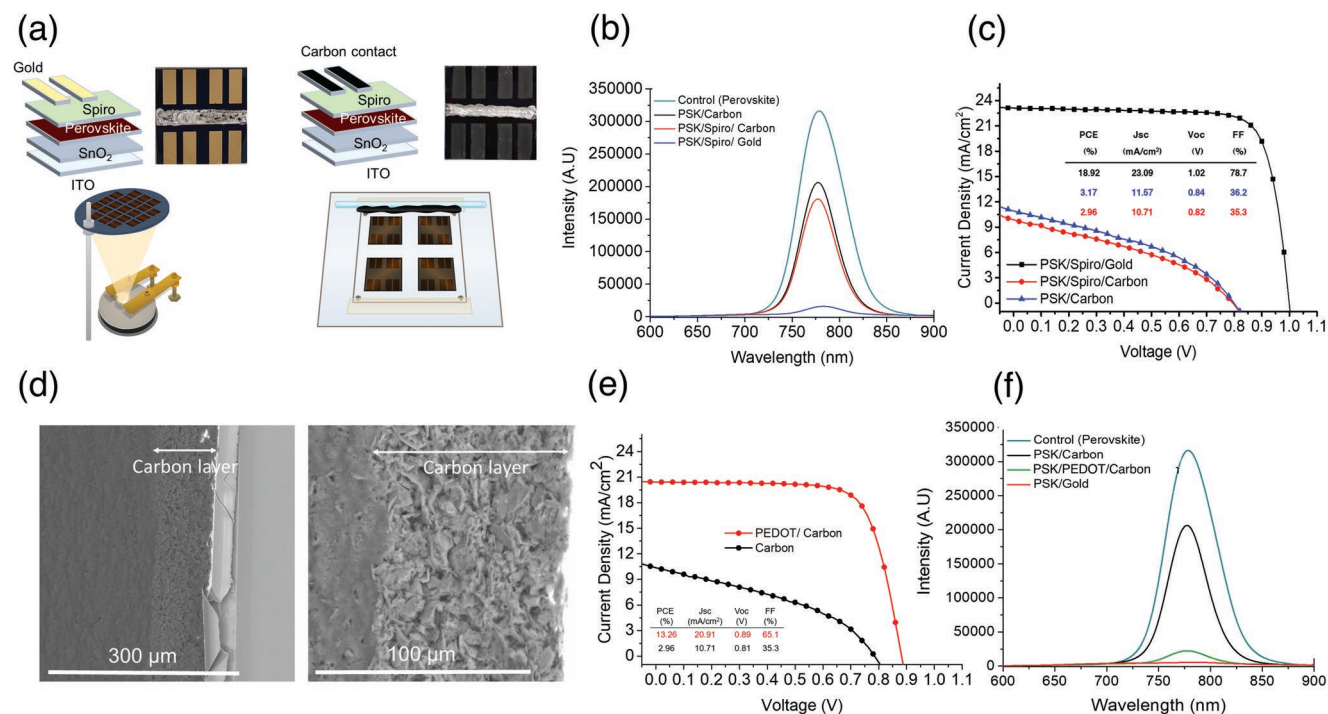
Figure 1. a) Schematic of stencil coating method and photograph of PSCs with carbon and gold top electrodes, b,c) steady-state PL spectra (b) and J–V curves (c) of perovskite/carbon, perovskite/spiro-MeOTAD/carbon, and perovskite/spiro/gold samples, d) cross-section SEM image of stencil coated carbon, and e,f) J–V curve (e) and steady-state PL spectra (f) of perovskite/carbon and perovskite/PEDOT/carbon.

Based on the results, charge transfer between perovskite and carbon directly has serious issues. Since the carbon layer has the low sheet resistance of 5.28 Ω sq^{-1} and the scanning electron microscopy (SEM) image of its morphology (Figure 1d) does not show many voids, it is likely that the charge-transfer issue is related to the interface between these two layers. On that account, we spin coated spiro-MeOTAD which is the most popular hole-transporting material to make the structure ITO/SnO$_2$/MAPI/Spiro/carbon, however a similar low PCE of 2.96% was achieved. Compared to spiro-MeOTAD/gold devices, steady-state photoluminescence (SSPL) measurements in Figure 1b show poor quenching further identifying the poor charge transfer between spiro-MeOTAD and carbon. This is an indication of poor compatibility between the HTL and the carbon ink formulation. From SSPL graphs and J–V curves similarity for samples with/without spiro-MeOTAD, it is determined that carbon ink incompatibility leads to dissolving/removing spiro layer underneath the carbon.

Afterward, commercially available and easy to coat PEDOT hole-transport material was employed as a substitute for spiro-MeOTAD. The J–V measurement results of Figure 1e prove that PEDOT replacement had a significant role on devices performance due to its compatibility with the carbon ink. The band energy schematic for this stack is shown in Figure S5 in the Supporting Information. The device efficiency reduced for evaporated gold electrodes, however it is greatly improved for stencil printed carbon electrodes achieving 13.25% champion (14.57% stabilized), full statistical data are in Figure S6 in

the Supporting Information also showing the consistency of the results. Moreover, SSPL measurement demonstrated efficient quenching (Figure 1f) suggesting the necessity of using PEDOT or any other equivalent compatible hole-transporting material between perovskite and the carbon top electrode. The results confirm that PEDOT not only acts an HTL compatible with carbon ink solvent, it is also intrinsically conductive aiding charge transfer to the printed carbon electrode minimizing recombination losses. It should be noted that the perovskite/gold interface shows improved SSPL quenching (Figure 1f) over perovskite/PEDOT/carbon and this along with increased back reflection may result in increased efficiency however as this would not be scalable through R2R coating it has not been investigated further. The compatibility of the carbon electrode with the device structure is further demonstrated by electrochemical impedance spectroscopy (EIS, **Figure 2**a), the series resistance derived from the Nyquist plots is remarkably low in value for gold and carbon electrodes (7.5 and 14.8 Ω, respectively) indicating good charge transfer at the electrode interfaces.

The corresponding external quantum efficiency (EQE) spectra of the three devices are shown in Figure 2b. As expected, due to its low charge extraction, the perovskite/carbon stack without interlayer has low EQE% (highest: ≈30%) in the whole wavelength range. Due to the fact that increase in overall QE curve is normally caused by higher charge extraction/lower recombination, by coating PEDOT between perovskite/carbon or perovskite/gold, the charge transfer from the absorbing
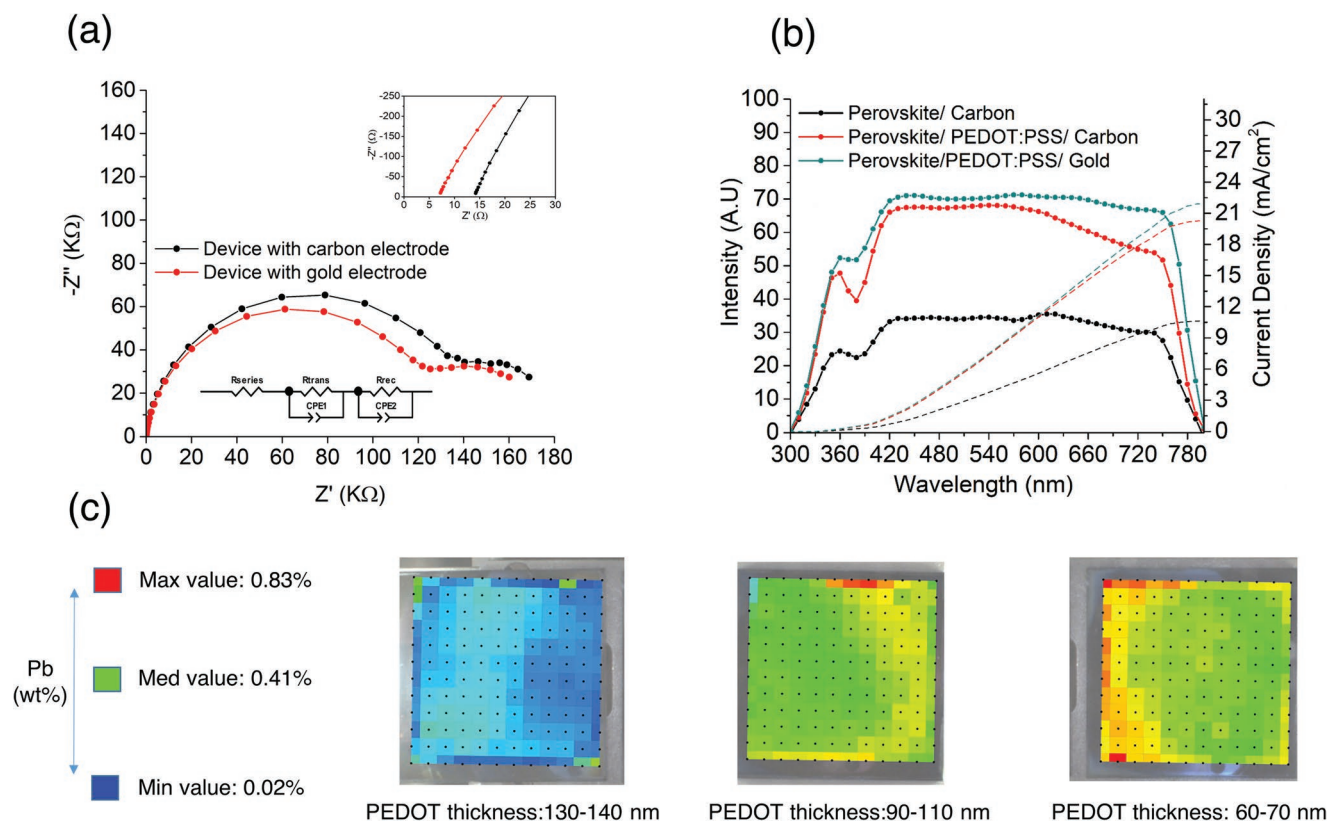
Figure 2. a) Nyquist plots and b) hero cell EQE spectra of device structures SnO$_2$/MAPI/carbon, SnO$_2$/MAPI/PEDOT/C, and SnO$_2$/MAPI/PEDOT/gold, and c) XPS spectra mapping of rigid PSCs with different thicknesses of PEDOT.

ADVANCED
SCIENCE NEWS

www.advancedsciencenews.com

ADVANCED
MATERIALS

www.advmat.de

layer toward the contact electrode is increased significantly. In the wavelength range 400–600 nm, both PEDOT/carbon and PEDOT/gold devices have relatively similar EQE%. However, from 600 to 700 nm there is a reduction in EQE observed for the PEDOT/carbon stack. Since the long wavelength response is related to the rear side of the device, this reduction explains the higher quality of interface and reflection between PEDOT/gold rather than PEDOT/carbon, which is to be expected.

In consideration of scaling up to R2R coating of the device structure, it is important to understand the optimal thickness of the PEDOT interlayer as thin coated layers will be susceptible to defects and more robust thicker layers detrimental to series resistance. PEDOT was coated with a thickness range from 60 to 140 nm with 90 nm found to be optimum (Figure S8, Supporting Information). X-ray photoelectron spectroscopy (XPS) lead elemental mapping of 28 × 28 mm ITO/SnO$_2$/MAPI/PEDOT-coated substrates reveals a narrow range of atomic lead (0.83% wt maximum) suggesting the perovskite is effectively covered with low defect occurrence at 90 nm thickness. Despite less perovskite being observed for the thicker deposition (130–140 nm), the lower defect rate does not result in improved efficiency (Figure 2C).

EIS has shown that charge transfer at the interface between PEDOT and carbon is comparable to PEDOT/gold and is confirmed by both the SSPL graphs and *J*–*V* data which demonstrate similar quenching and PV performance (**Figure 3**a,b). This confirms that the carbon electrode used in this study is an exceptional alternative to gold however this is only achieved following development of device structure, formulation, and processing optimization (Figure 3c). Initially device efficiency of ≈3% was achieved with only carbon (HTL free) and spiro-MeOTAD-based cells, a modest improvement was made by optimizing the carbon electrode formulation but by introducing the PEDOT HTL and then optimizing PEDOT thickness (Figures S7 and S8, Supporting Information), efficiency was increased to 12.5%, final parameter optimization for the stencil-coated carbon electrode resulted in the optimized device efficiency of 14.57%.

Typically conventional PEDOT:PSS as an interlayer is known to be hygroscopic and likely to introduce poor device stability, this instability is commonly attributed to the PSS counterion.[51] However, stability testing demonstrates the commercially available HTL Solar 3 PEDOT, which uses an alternative sulfonated block co-polymer[52] to PSS, when used in the PEDOT/carbon system counteracts any prior instabilities observed. PEDOT/carbon and PEDOT/gold devices with no encapsulation under 70%RH (relative humidity)/25 °C conditions have long-term stability of 80% retained efficiency over 1000 h compared to the conventional spiro-MeOTAD samples that lost 50% of their efficiency over the same time scale (Figure 3d).

The additional protection afforded by the carbon electrode is revealed in high-humidity/temperature conditions. Thermal/humidity testing at 65 °C/85% RH under dark condition (ISOS D3) shows high stability for unencapsulated carbon electrode devices compared to evaporated gold electrodes, Figure 3e. The device architectures with evaporated gold electrode are outperformed by the PEDOT/carbon electrode as the spiro/Au and PEDOT/Au decline to 20% and 40% of their original PCE within the first 15 min, while the PEDOT/carbon devices retain over 85% of the original efficiency for the duration of testing (60 min). It is possible that the thick (≈25 µm) hydrophobic carbon electrode is acting as a pseudo-encapsulant protecting the perovskite from degradation.

2.2. Fully R2R Devices

In spite of the fact that most of the studies in the field of nanostructured solar cells have been focused on performance development of the devices, in recent years a few promising breakthrough reports have centered on scaling-up of these devices, specifically through R2R coating (Table 1).

However, as of the time of writing this paper, none have reported fabrication of a whole R2R structure device including the top electrode. Inclusion of a solution R2R processed electrode is an important advancement as it enables, when combined with R2R encapsulation, the fabrication of large volumes of complete perovskite photovoltaics in a single high-speed process a key enabler in transitioning the many advancements in the perovskite research from the laboratory to the factory (lab to fab).

Since the prototype carbon electrode devices revealed the same performance results as gold electrodes, we transferred to R2R coating with carbon ink modified for low-viscosity compatible with slot-die coating. Flexible substrate-based n–i–p devices were prepared by using a prepatterned 100 mm-wide PET roll coated with ITO (sheet resistance of 50 Ω sq^{-1}).

Figure 4 represents a schematic of the R2R coating process conducted with a Cotema Smartcoater. The procedure for each slot-die-coated layer includes three continuous steps: coating, annealing, and rewinding of the substrate in preparation for the next layer coating. All device layers were sequentially slot-die coated at a common coating speed of 1 m min^{-1} along with passing through ovens with a total length of 1 m, at completion of coating no further processing was needed to complete the device structure. The definition of coating parameters for tin oxide, perovskite, PEDOT, and carbon ink can be found in the Experimental Section and a video showing R2R coating is available in the Supporting Information.

The functionality of the R2R-coated devices has been examined using electroluminescence (EL) emission tests. In the case of having a flawless structure, electrical phenomenon would convert to light emission in response to the passage of electricity through the device, with brighter areas indicating better performing zones of the device. However, having flaws on some parts/points in each layer will lead to cessation of illumination on that area or even electrical disconnection between both sides of the circuit and will result in darkness for the whole device. **Figure 5**a shows a flexible stencil-coated carbon electrode device. As can be seen three out of four stripes of small-scale stencil-coated device were working well and one had issues on its corner illustrating a coating defect. Furthermore, the photograph of a random cut device sample from our slot-die-coated R2R solar cell is shown in Figure 5b. The illumination along the length of the electrode indicates that there are no disruptive defects along them.

To ensure our R2R developed carbon ink is completely compatible with the perovskite layer underneath, X-ray diffraction

**ADVANCED
SCIENCE NEWS**

www.advancedsciencenews.com

**ADVANCED
MATERIALS**

www.advmat.de
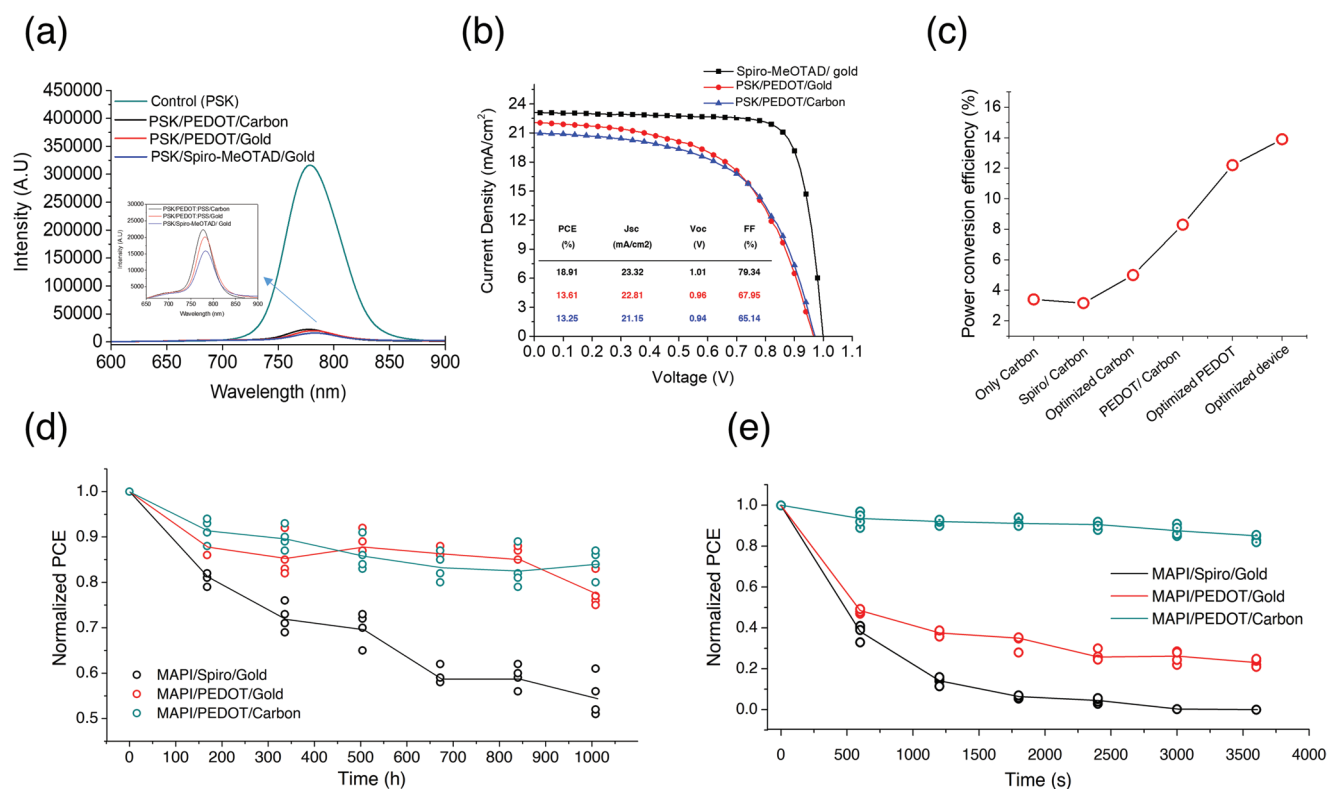
Figure 3. a,b) Steady-state PL spectra and hero cell *J–V* curves of MAPI/PEDOT/C, MAPI/PEDOT/Au, and MAPI/Spiro-MeOTAD/Au structures, c) photovoltaic performance development pathway of PSCs with carbon top electrode, d) humidity stability test under 70% RH at 25 °C, and e) thermal/humidity stability test under 85% RH at 65 °C for carbon and gold top electrode devices.

(XRD) analysis was employed. For appropriate comparison, three device structures were employed, the full device stack including PEDOT and carbon applied using both stencil coating and R2R slot-die coating was then compared to perovskite (MAPI) coated on tin oxide as a pristine control. Relative peak intensity of the XRD spectra shows that stencil-coated carbon
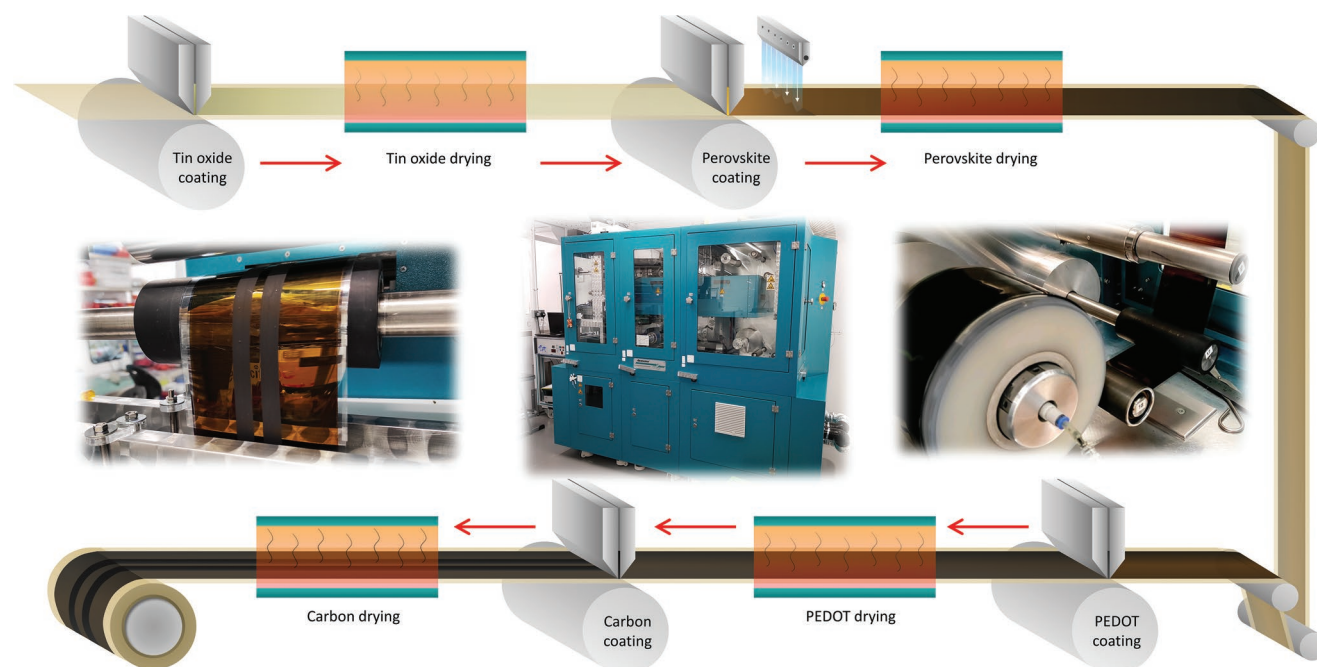
Figure 4. Schematic visualization of R2R slot-die coating method for fabrication of PSCs with carbon top electrode.

2208561 (6 of 10)

(a)

(b)
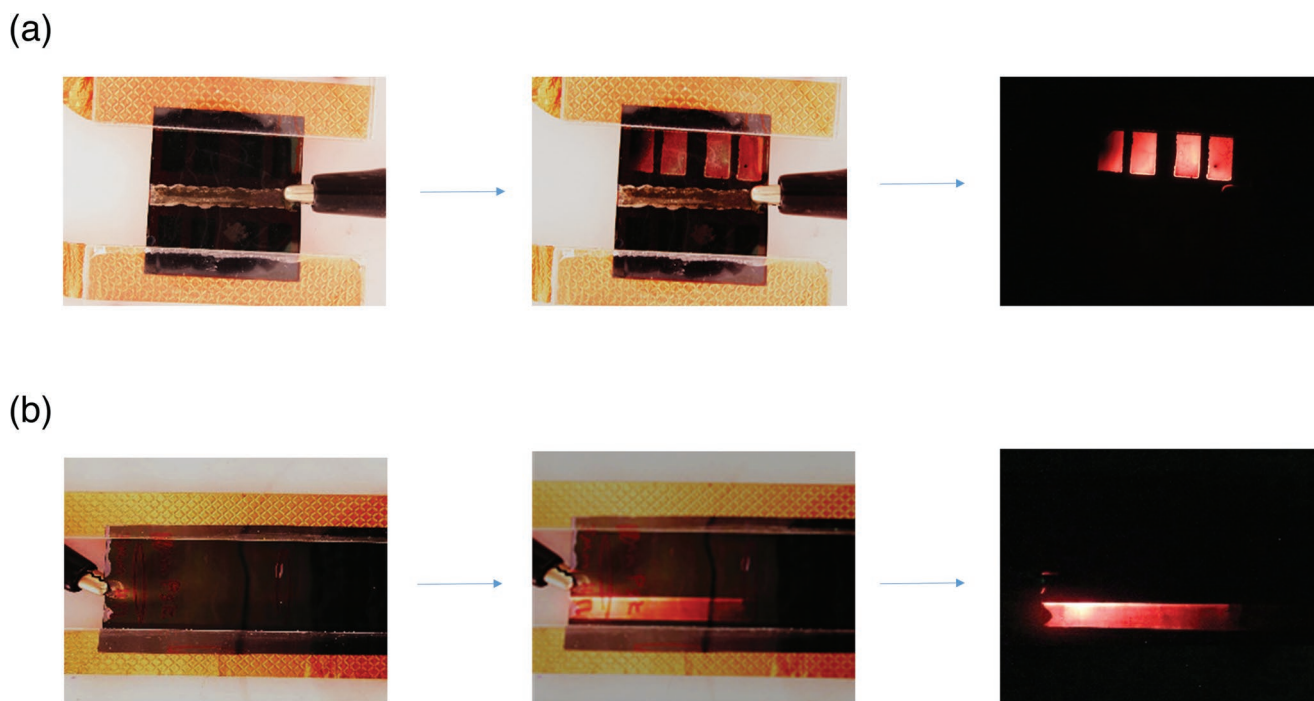
Figure 5. a,b) EL emission photography of small-scale flexible PSCs (a) and R2R carbon electrode PSCs (b). Images in the middle are superposition of the images on the left and on the right. Also, images on the left are captured under illumination, no-bias applied. The images in the right are taken in the dark under bias.

samples and R2R devices have similar PbI_2 concentrations relative to the MAPI peak, slightly lower than the pristine MAPI sample (**Figure 6**a). This suggests that not only are the carbon inks used for stencil coating and R2R slot die compatible with MAPI but they have also shown protective properties against its degradation (Table S1, Supporting Information). Furthermore, the sequential R2R drying processes inside the ovens have not degraded the perovskite with crystallite size of 50–90 nm, which is another sign of successful coating of carbon.

Cross-section field-emission SEM (FE-SEM, Figure 6b1) and focused ion beam (FIB)-SEM (Figure 6b2) images of R2R slot-die-coated devices show the carbon ink forms a compact layer free of voids that may be formed by solvent entrapment, the carbon electrode makes intimate conformal contact with the underlying PEDOT layer. XPS elemental lead mapping of R2R-coated SnO_2/MAPI/PEDOT (Figure 6c) indicates that the coverage is effective and covers high points so as to prevent pinhole/shorting defects. The % lead in the XPS map is lower than identified in optimum spin-coated devices (Figure 2c) highlighting the increased requirement to cover defects in R2R slot die compared to spin coating.

In order to test the 20 m-long R2R printed device, the substrate was manually diced into segments similar in size to our small-scale devices and randomly selected samples were measured conventionally. Sections without printed carbon electrode were also collected and gold electrode was evaporated, although a light soaking effect was observed for the carbon electrodes, the measurement protocol was maintained for both gold and carbon electrode devices. The R2R perovskite devices using gold evaporated electrode had a high PCE of 13.21% (12.87% stabilized PCE) comparable to the highest performing

evaporated electrode R2R devices reported. For fully printed carbon electrode cells, a PCE of 9.79% (10.84% stabilized PCE) was achieved.

Based on J–V curve of hero cells in Figure 6d and statistical data of box plots presented in Figure S9 in the Supporting Information, both fully R2R and R2R/gold devices have very close values for current density and open circuit voltage. However, fully R2R devices have shown lower fill factor compared to evaporated gold samples leading to lower PCEs. Moreover, it should be noted that although the performance of devices with PEDOT/carbon compared to spiro-MeOTAD/carbon is improved, it still suffers from the lack of appropriate fill factor compared to the conventional spiro-MeOTAD/gold devices. PEDOT is not the only compatible candidate carbon electrode interlayer but it has proven effective to make the first demonstration of fully R2R-coated perovskite device. This strategy in combination with the compatible carbon ink formulation can be further extended to even better hole-transport/interlayer materials in principle to achieve higher performance fully R2R-coated perovskite.

3. Conclusion

This work presents a significantly low-cost and scalable carbon ink formulation replacing the conventional expensive lab-scale metal top electrodes. Further, we demonstrate the tremendous impact of a PEDOT layer on the perovskite/HTL/carbon interface modification. Benefiting from the combination of this HTL with our slot-die-compatible carbon ink, we fabricated the world's first fully R2R flexible PSCs. The prototype carbon
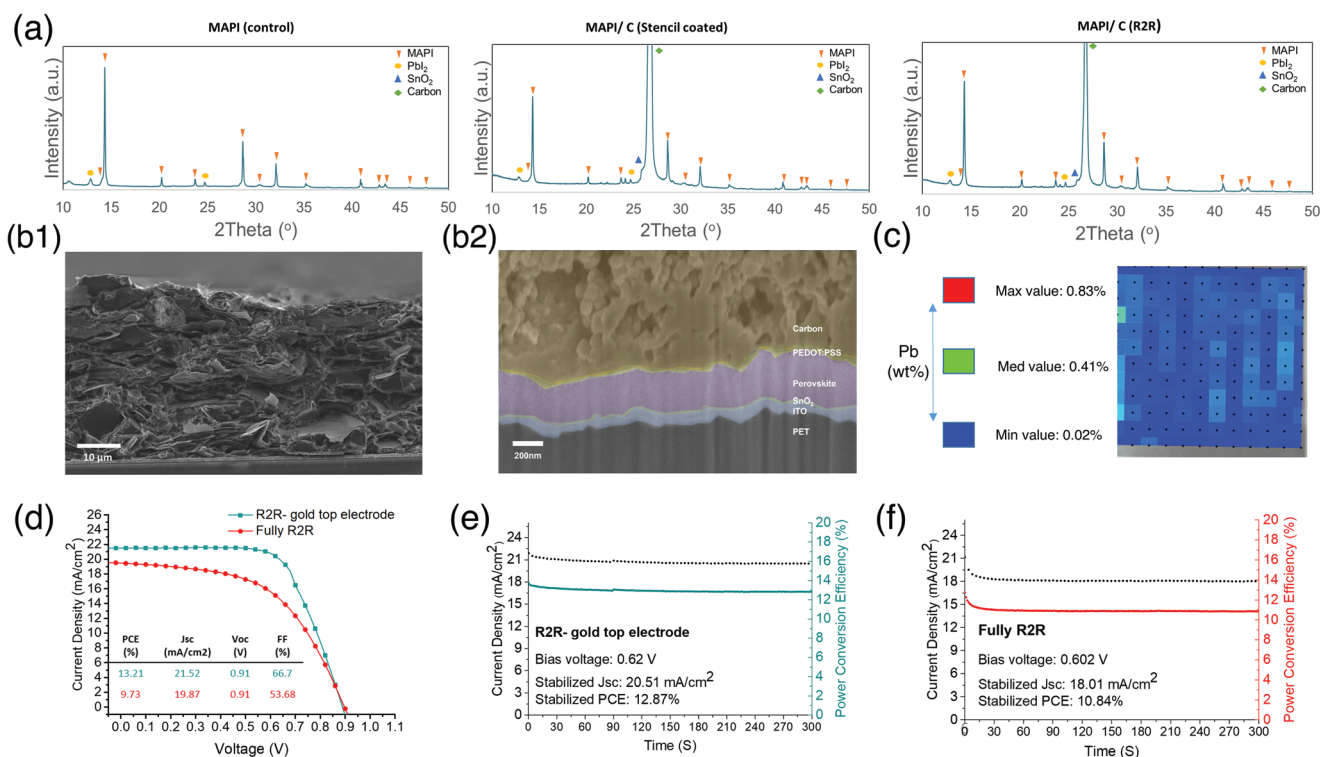
Figure 6. a) XRD spectra of MAPI (control), carbon stencil-coated, and R2R-coated samples, b) cross-section FE-SEM, c) XPS spectra of PSCs with R2R v stencil carbon electrodes, and d–f) J–V and J–t curves of R2R PSCs with evaporated gold versus fully R2R structure.

electrode small-scale devices on rigid glass substrates obtained a PCE of 13.25% and then extended to a fully R2R coating system with 20 m-long flexible substrates to yield the stabilized PCE of 10.8%. More importantly, devices fabricated with carbon electrodes provided similar photovoltaic performance as conventional evaporated gold electrodes with the hero device PCE of 13.26% and 13.61%, respectively. Moreover, spin-coated devices where the carbon ink was applied using stencil printing showed better long-term stability rather than gold, however, these devices have shown significantly more stability under severe thermal/humidity conditions. The use of PEDOT/carbon electrodes in R2R perovskite devices has been demonstrated to be an operational alternative to conventional expensive nonscalable spiro-MeOTAD/gold electrodes. This achievement is a leap forward in reaching the promise of perovskite photovoltaics in printing millions of meters of solar cells worldwide.

4. Experimental Section

Materials: Unless mentioned otherwise, all chemicals and solvents including lead iodide (PbI_2, TCI chemicals, 99.99%), methylammonium iodide (MAI, greatcell solar, >99% anhydrous), tin (iv) oxide colloidal dispersion liquid (Alfa Aesar, 15% in H_2O), PEDOT (HTL SOLAR3, Ossila), carbon black nanosize primary particles (Imerys, Ensaco), synthetic graphite (Imerys, Timrex), 1-butanol (Scientific Laboratory Supplies, 99.8% anhydrous), methylamine solution (Fisher Scientific, 33% in ethanol), and 2-methylanisole (Alfa Aesar, >99%) were purchased and used without further purifications. Other chemicals and solvents including spiro-MeOTAD powder (high-performance liquid chromatography, 99%), lithium bis(trifluoromethylsulfonyl)imide salt (Li-TFSI, 99.99%), 4-*tert*-butylpyridine (t-BP, 96%), and FK209 Co(iii) TFSI

salt, ethyl cellulose, acetonitrile (99.8% anhydrous), and chlorobenzene (99.8% anhydrous) were all purchased from Sigma-Aldrich.

Rigid Device Fabrication: ITO glass substrates (sheet resistance ≈15 Ω sq^{-1}) were washed/cleaned in an ultrasonic cleaner for 10 min each, with hellmanex cleaning concentrate (2% in deionized (DI) water), DI water, acetone, and 2-propanol, respectively. After drying by N_2 blowing, the substrates were treated with UV–ozone cleaner for 15 min in regards of increase in their surface energy and wetting ability. To deposit the electron-transporting layer, tin(IV) oxide 15% in H_2O colloidal dispersion diluted with water (4.2% wt SnO_2) and then spin coated at 4000 rpm for 30 s and annealed at 150 °C for 30 min.

Following this, the 0.73 M perovskite solution was filtered by a 0.2 µm PTFE syringe filter and deposited at 3000 rpm for 60 s, then annealed at 120 °C for 10 min .The preparation details of perovskite MAPI solution in acetonitrile can be found in previous work.[26] Then, on top of perovskite absorbing layer, PEDOT solution (in toluene) was spin coated at 3000 rpm for 40 s and annealed at 110 °C for 10 min. For devices with spiro-MeOTAD as HTL, 90 mg mL^{-1} spiro powder was dissolved in chlorobenzene. Then, 20 µL LiTFSI (520 mg mL^{-1} in acetonitrile (ACN)), 30 µL 4-*tert*-butylpyridine, and 10 µL FK209 (300 mg mL^{-1} in ACN) were added as additives and the final prepared solution was stirred at 60 °C. The prepared solution was then spin coated at 4000 rpm for 30 s without further annealing. Finally, Au was evaporated on the HTL as the top electrode. For devices with carbon electrode, carbon ink was coated by stencil coating and then dried at 110 °C for 10 min. The stencil design and evaporation mask were identical therefore for both gold and carbon electrode producing eight 4 mm × 10 mm cells (0.15 cm^2 active area over ITO). A modest device size and masking process was employed in order to focus specifically on the behavior of the carbon from a processing and compatibility perspective. Future larger area deposition of the carbon should also incorporate elements of module design and interconnect to progress the technology further.

Carbon Ink Preparation: Ethyl cellulose and 2-methylanisole were weighed and mixed under high shear using a Speedmixer twice at 3500 rpm for 5 min, the solution was left for 24 h to ensure the binder

was fully dissolved. Commercially sourced carbon black (0.77 g stencil ink, 0.34 g slot-die ink) and graphite (2 g stencil ink, 0.88 g slot-die ink) components were then weighed into the resin and again mixed in the Speedmixer (2 × 3500 rpm for 5 min) followed by standing for 24 h to allow solvent absorption by the carbon and achieve the final viscosity of the ink. The carbon black material was supplied as an agglomeration of nanosized primary particles and graphite as aggregate of micrometer size (D90 6 μm) flakes therefore, the ink was again mixed twice at 3500 rpm for 5 min breaking any remaining agglomerates and ensuring a smooth and well-combined ink.

R2R Devices Fabrication: Device layers were sequentially slot-die coated onto 50 Ω sq^{-1} ITO at a common speed of 1 m min^{-1} using a Cotema Smartcoater R2R coating system. Tin oxide (Alpha Aesar) was diluted to 1.2% wt with DI water and 10% 1-butanol was coated at 90 mm width and 5–11 μm (7 μm optimum) wet film thickness with 1 mm meniscus guide, 200 μm gap, and 140 °C drying temperature. Next perovskite solution (as used in rigid device fabrication) was coated at 90 mm width and 3–9 μm (7 μm optimum) wet film thickness, 1 mm meniscus guide, 200 μm gap, an airknife was employed directly following coating with 50 L min^{-1} nitrogen flow, then dried at 150 °C oven setpoint. PEDOT (HTL solar 3) was coated as supplied at 3–6 μm (4 μm optimum) wet film thickness and 90 mm width using a 0.25 mm meniscus guide, 150 μm gap, and 140 °C drying temperature. Two stripes of 3 mm-wide carbon ink were coated to define the electrode pattern over 20 mm-wide patterned ITO defining an active area of 0.6 cm^2, no meniscus guide was used, coating thickness was 250 μm wet film, and oven setpoint was 140 °C. Oven residence time for all coated layers was 1 min.

Characterization: For full devices photovoltaic performance measurements, a Keithley 2400 source meter and a solar simulator (Newport oriel Sol3A) was used. *J–V* and stabilized current (*J–t*) curves (for a period of 300 s) were measured at 1 sun after calibration. The active area was 0.09 cm^2 for all devices, which was defined by a mask on top of the measuring module. EQE curves were measured as a function of wavelength range 300–800 nm on a custom-build system consisting of Xenon arc and Quartz halogen white-light sources and a Bentham TMc300 monochromator. Steady-state PL spectra were obtained using FS5 spectrofluorometer Edinburgh instrument with an excitation wavelength of 430 nm and a 496 nm long-pass filter in the emission pathway. Thicknesses of layers were measured using a KLA Tencor D-600 profilometer. For measuring the thickness of layers on flexible substrates, an air table was used to avoid any vibration during the measurement, which in turn reduced noises in resultant profile. The morphology of films grown on a glass substrate was studied using a Hitachi TM3000 desktop SEM and JEOL-JSM-7800F FE-SEM (5 kV acceleration voltage, a working distance of 10 mm, and a magnification of ×1500). The cross-section of films grown on a PET substrate was achieved in a Zeiss Crossbeam 550 FIB Field emission gun - scanning electron microscope. The Ga source FIB was operated in standard configuration with the sample surface perpendicular to the ion beam, tilted 54° to the electron beam column. A high current 30 kV 15 nA probe was used to rough trench the area, before the cross-section face was developed using lowering 30 kV probes to 30 kV 700 pA and a 55.4° tilt. The images then were recorded with InLens secondary electron detector and backscattered electron images were achieved with a filtered ESB detector. The XPS analysis was carried out using a Kratos axis supra XPS equipped with a minibeam 6-gas cluster ion source. XRD scans were undertaken using a Bruker D8 advance instrument using a copper source, in Bragg–Brentano geometry, between 10° and 50° with a 0.02° step size and time of 1 s per step. EIS analysis was performed using a Zahner CIMPs-X photoelectrochemical workstation to attain the Nyquist plots of the equivalent circuit used for impedance and capacitance data. Measurements were performed under dark situation over the frequency range 1 MHz to 1 Hz at potentiostat DC voltage of 0.8 V. The EL images were taken with a modified Canon EOS 600D camera without IR filters in the dark while a constant voltage was applied to the devices with a RS Pro Bench Power Supply.

Supporting Information

Supporting Information is available from the Wiley Online Library or from the author.

Conflict of Interest

The authors declare no conflict of interest.

Data Availability Statement

The data that support the findings of this study are available from the corresponding author upon reasonable request.

[1] Y. S. Jung, K. Hwang, Y. J. Heo, J. E. Kim, D. Vak, D. Y. Kim, *Adv. Opt. Mater.* **2018**, *6*, 1701182.

[2] Y. Li, H. Xie, E. L. Lim, A. Hagfeldt, D. Bi, *Adv. Energy Mater.* **2022**, *12*, 2102730.

[3] T. Webb, S. J. Sweeney, W. Zhang, *Adv. Funct. Mater.* **2021**, *31*, 2103121.

[4] A. Kojima, K. Teshima, Y. Shirai, T. Miyasaka, *J. Am. Chem. Soc.* **2009**, *131*, 6050.

[5] H.-S. Kim, C.-R. Lee, J.-H. Im, K.-B. Lee, T. Moehl, A. Marchioro, S.-J. Moon, R. Humphry-Baker, J.-H. Yum, J. E. Moser, *Sci. Rep.* **2012**, *2*, 591.

[6] M. Liu, M. B. Johnston, H. J. Snaith, *Nature* **2013**, *501*, 395.

[7] J. J. Yoo, G. Seo, M. R. Chua, T. G. Park, Y. Lu, F. Rotermund, Y.-K. Kim, C. S. Moon, N. J. Jeon, J.-P. Correa-Baena, *Nature* **2021**, *590*, 587.

[8] G.-H. Kim, D. S. Kim, *Joule* **2021**, *5*, 1033.

[9] D. Li, D. Zhang, K. S. Lim, Y. Hu, Y. Rong, A. Mei, N. G. Park, H. Han, *Adv. Funct. Mater.* **2021**, *31*, 2008621.

[10] F. Yang, D. Jang, L. Dong, S. Qiu, A. Distler, N. Li, C. J. Brabec, H. J. Egelhaaf, *Adv. Energy Mater.* **2021**, *11*, 2101973.

[11] K. Hwang, Y. S. Jung, Y. J. Heo, F. H. Scholes, S. E. Watkins, J. Subbiah, D. J. Jones, D. Y. Kim, D. Vak, *Adv. Mater.* **2015**, *27*, 1241.

**ADVANCED
SCIENCE NEWS**
www.advancedsciencenews.com

**ADVANCED
MATERIALS**
www.advmat.de

[12] R. Swartwout, R. Patidar, E. Belliveau, B. Dou, D. Beynon, P. Greenwood, N. Moody, D. DeQuilettes, M. Bawendi, T. Watson, *Sol. RRL* **2022**, *6*, 2100567.

[13] D. Angmo, G. DeLuca, A. D. Scully, A. S. Chesman, A. Seeber, C. Zuo, D. Vak, U. Bach, M. Gao, *Cell Rep. Phys. Sci.* **2021**, *2*, 100293.

[14] J. Li, J. Dagar, O. Shargaieva, M. A. Flatken, H. Köbler, M. Fenske, C. Schultz, B. Stegemann, J. Just, D. M. Többens, *Adv. Energy Mater.* **2021**, *11*, 2003460.

[15] I. Zimmermann, M. Al Atem, O. Fournier, S. Bernard, S. Jutteau, L. Lombez, J. Rousset, *Adv. Mater. Interfaces* **2021**, *8*, 2100743.

[16] S. H. Huang, C. K. Guan, P. H. Lee, H. C. Huang, C. F. Li, Y. C. Huang, W. F. Su, *Adv. Energy Mater.* **2020**, *10*, 2001567.

[17] F. Xu, J. Liu, A. S. Subbiah, W. Liu, J. Kang, G. T. Harrison, X. Yang, F. H. Isikgor, E. Aydin, M. De Bastiani, *Small Sci.* **2021**, *1*, 2000044.

[18] D. Burkitt, P. Greenwood, K. Hooper, D. Richards, V. Stoichkov, D. Beynon, E. Jewell, T. Watson, *MRS Adv.* **2019**, *4*, 1399.

[19] R. Patidar, D. Burkitt, K. Hooper, D. Richards, T. Watson, *Mater. Today Commun.* **2020**, *22*, 100808.

[20] H. Li, C. Zuo, A. D. Scully, D. Angmo, J. Yang, M. Gao, *Flexible Printed Electron.* **2020**, *5*, 014006.

[21] J. E. Kim, S. S. Kim, C. Zuo, M. Gao, D. Vak, D. Y. Kim, *Adv. Funct. Mater.* **2019**, *29*, 1809194.

[22] T. M. Schmidt, T. T. Larsen-Olsen, J. E. Carlé, D. Angmo, F. C. Krebs, *Adv. Energy Mater.* **2015**, *5*, 1500569.

[23] Z. Gu, L. Zuo, T. T. Larsen-Olsen, T. Ye, G. Wu, F. C. Krebs, H. Chen, *J. Mater. Chem. A* **2015**, *3*, 24254.

[24] H. Li, C. Zuo, D. Angmo, H. Weerasinghe, M. Gao, J. Yang, *Nano-Micro Lett.* **2022**, *14*, 79.

[25] M. Othman, F. Zheng, A. Seeber, A. S. Chesman, A. D. Scully, K. P. Ghiggino, M. Gao, J. Etheridge, D. Angmo, *Adv. Funct. Mater.* **2022**, *32*, 2110700.

[26] D. Burkitt, R. Patidar, P. Greenwood, K. Hooper, J. McGettrick, S. Dimitrov, M. Colombo, V. Stoichkov, D. Richards, D. Beynon, *Sustainable Energy Fuels* **2020**, *4*, 3340.

[27] L. J. Sutherland, D. Vak, M. Gao, T. A. N. Peiris, J. Jasieniak, G. P. Simon, H. Weerasinghe, *Adv. Energy Mater.* **2022**, *12*, 2202142.

[28] C. Zuo, D. Vak, D. Angmo, L. Ding, M. Gao, *Nano Energy* **2018**, *46*, 185.

[29] Y. Galagan, F. Di Giacomo, H. Gorter, G. Kirchner, I. de Vries, R. Andriessen, P. Groen, *Adv. Energy Mater.* **2018**, *8*, 1801935.

[30] B. Dou, J. B. Whitaker, K. Bruening, D. T. Moore, L. M. Wheeler, J. Ryter, N. J. Breslin, J. J. Berry, S. M. Garner, F. S. Barnes, *ACS Energy Lett.* **2018**, *3*, 2558.

[31] C. Gong, S. Tong, K. Huang, H. Li, H. Huang, J. Zhang, J. Yang, *Sol. RRL* **2020**, *4*, 1900204.

[32] Y. Y. Kim, T.-Y. Yang, R. Suhonen, A. Kemppainen, K. Hwang, N. J. Jeon, J. Seo, *Nat. Commun.* **2020**, *11*, 5146.

[33] G. A. Sepalage, H. Weerasinghe, N. Rai, N. W. Duffy, S. R. Raga, Y. Hora, M. Gao, D. Vak, A. S. Chesman, U. Bach, *Adv. Mater. Technol.* **2022**, *7*, 2101148.

[34] J. F. Benitez-Rodriguez, D. Chen, A. D. Scully, C. D. Easton, D. Vak, H. Li, P. E. Shaw, P. L. Burn, R. A. Caruso, M. Gao, *Sol. Energy Mater. Sol. Cells* **2022**, *246*, 111884.

[35] Y. Y. Kim, T. Y. Yang, R. Suhonen, M. Välimäki, T. Maaninen, A. Kemppainen, N. J. Jeon, J. Seo, *Adv. Sci.* **2019**, *6*, 1802094.

[36] F. Bisconti, A. Giuri, R. Suhonen, T. M. Kraft, M. Ylikunnari, V. Holappa, P. Biagini, A. Savoini, G. Marra, S. Colella, *Cell Rep. Phys. Sci.* **2021**, *2*, 100639.

[37] M. Que, B. Zhang, J. Chen, X. Yin, S. Yun, *Mater. Adv.* **2021**, *2*, 5560.

[38] S. M. Meroni, C. Worsley, D. Raptis, T. M. Watson, *Energies* **2021**, *14*, 386.

[39] C. Worsley, D. Raptis, S. Meroni, R. Patidar, A. Pockett, T. Dunlop, S. Potts, R. Bolton, C. Charbonneau, M. Carnie, *Mater. Adv.* **2022**, *3*, 1125.

[40] S. Wang, P. Jiang, W. Shen, A. Mei, S. Xiong, X. Jiang, Y. Rong, Y. Tang, Y. Hu, H. Han, *Chem. Commun.* **2019**, *55*, 2765.

[41] M. Bidikoudi, C. Simal, E. Stathatos, *Electronics* **2021**, *10*, 1145.

[42] D. Bogachuk, B. Yang, J. Suo, D. Martineau, A. Verma, S. Narbey, M. Anaya, K. Frohna, T. Doherty, D. Müller, *Adv. Energy Mater.* **2022**, *12*, 2103128.

[43] F. Yang, L. Dong, D. Jang, B. Saparov, K. C. Tam, K. Zhang, N. Li, C. J. Brabec, H. J. Egelhaaf, *Adv. Energy Mater.* **2021**, *11*, 2101219.

[44] H. Zhang, J. Xiao, J. Shi, H. Su, Y. Luo, D. Li, H. Wu, Y. B. Cheng, Q. Meng, *Adv. Funct. Mater.* **2018**, *28*, 1802985.

[45] X. Wu, L. Xie, K. Lin, J. Lu, K. Wang, W. Feng, B. Fan, P. Yin, Z. Wei, *J. Mater. Chem. A* **2019**, *7*, 12236.

[46] V. Babu, R. F. Pineda, T. Ahmad, A. O. Alvarez, L. A. Castriotta, A. Di Carlo, F. Fabregat-Santiago, K. Wojciechowski, *ACS Appl. Energy Mater.* **2020**, *3*, 5126.

[47] C. Zhang, S. Wang, H. Zhang, Y. Feng, W. Tian, Y. Yan, J. Bian, Y. Wang, S. Jin, S. M. Zakeeruddin, *Energy Environ. Sci.* **2019**, *12*, 3585.

[48] G. A. Sepalage, H. Weerasinghe, N. Rai, N. W. Duffy, S. R. Raga, Y. Hora, M. Gao, D. Vak, A. S. Chesman, U. Bach, A. N. Simonov, *Adv. Mater. Technol.* **2021**, *7*, 2101148.

[49] D. Richards, D. Burkitt, R. Patidar, D. Beynon, T. Watson, *Mater. Adv.* **2022**, *3*, 8588.

[50] D. Burkitt, R. Swartwout, J. McGettrick, P. Greenwood, D. Beynon, R. Brenes, V. Bulović, T. Watson, *RSC Adv.* **2019**, *9*, 37415.

[51] Y. Xia, G. Yan, J. Lin, *Nanomaterials* **2021**, *11*, 3119.

[52] J. Liu, S. Pathak, T. Stergiopoulos, T. Leijtens, K. Wojciechowski, S. Schumann, N. Kausch-Busies, H. J. Snaith, *J. Phys. Chem. Lett.* **2015**, *6*, 1666.

2208561 (10 of 10)